Thermal cure Coupling Optimization Analysis of Integrated Thermal Protection System Connector

Bin Wang [1], Dongqiang Zhao [1], Yu Ning [1, *], Cunxian Wang [1, 2], Peng Du [1], and Feng Xiong [1]

[1] AVIC the First Aircraft Institute, Xi'an 710089, China
[2] Northwestern Polytechnical University, Xi'an 710089, China
*Corresponding author's e-mail: nwpuwb@163.com

Abstract. This study focuses on the heat conduction characteristics and stress distribution patterns of the Z-shaped connecting bracket in thermal protection structures. A two-dimensional heat conduction model is established, considering the thermal radiation interaction between the outer panel and the external environment. By simulating heat conduction under different insulation layer thicknesses, the relationship between the maximum temperature of the base panel and insulation layer thickness is revealed. The model's accuracy is verified through comparisons with a three-dimensional model and actual temperature data. Furthermore, a 1/8 scale model of the thermal protection structure is established to analyze the impact of pressure loads on bracket stress, identifying the main causes of high-stress areas. The temperature gradient in the structure's thickness direction is found to be a key factor causing higher stress on the bracket. This research proposes a novel numerical approach for the design and optimization of thermal protection structures in aerospace vehicles.

Keywords: Connector; Z-shaped; Stress; Thermal analysis

1   Introduction

In the exploration of outer space, reusable launch vehicles (RLVs) play a crucial role due to their multifunctionality [1], making them a significant focus of high-tech development in several developed countries. Since the 1980s, countries around the world have been actively researching RLVs [2]. Although some countries have temporarily suspended certain aerospace plane projects in recent years due to funding issues, it is undeniable that reusable aerospace planes indeed hold the potential to significantly reduce launch costs on a large scale in future developments [3].

As one of the most critical components of spacecraft, the thermal protection structure shields the internal components from the high temperatures encountered during reentry into the Earth's atmosphere [4]. The thermal protection system faces complex loads during atmospheric reentry, including thermal, acoustic, and vibrational challenges, which trouble researchers in the design of aircraft thermal protection structures [5]. The issues related to high-temperature stresses induced by thermal flux loads are particularly significant [6].

Thermal protection structures for aerospace vehicles primarily consist of three main types: passive, semi-passive, and active [7]. The latter two types can withstand high temperatures but involve complex structures and high manufacturing and maintenance costs, so they are less commonly used or limited to high-temperature areas like the nose of the spacecraft. In contrast, passive thermal protection systems are simpler in structure and easier to manufacture and maintain [8]. Among passive systems, the tile-based structure with insulation layers is particularly favored by designers [9]. This type of structure effectively isolates high temperatures from penetrating the internal structure of the aerospace vehicle [10].

Passive thermal protection systems, specifically those using insulation layer-based structures, consist of a thermal structure on the outer layer and a cold structure within the airframe frame. The connection between the cold and thermal structures often experiences stress concentration due to thermal mismatch and temperature gradients. In severe cases, this can adversely affect the safety and lifespan of the spacecraft. Historically, there have been two catastrophic accidents involving aerospace vehicles, resulting in loss of life and destruction of the craft. Subsequent investigations revealed a direct correlation between these accidents and the thermal protection systems along with their associated connecting structures.

The Z-shaped bracket, as a relatively simple connection between external panels and internal structures, has been studied extensively by scholars, as shown in Figure 1. Blosser et al. applied the Z-shaped bracket in metal thermal protection systems and investigated its deformation under thermal loads [11]. H. Böhrk and Beyermann utilized ceramic matrix composite materials for Z-shaped brackets and employed composite material bolts to mitigate thermal mismatch issues [12]. Z-shaped brackets are convenient to disassemble, straightforward to apply, and are considered a favorable choice for the connection between internal and external structures in removable thermal protection systems. However, systematic studies on the structural dimensions of Z-shaped brackets are lacking.
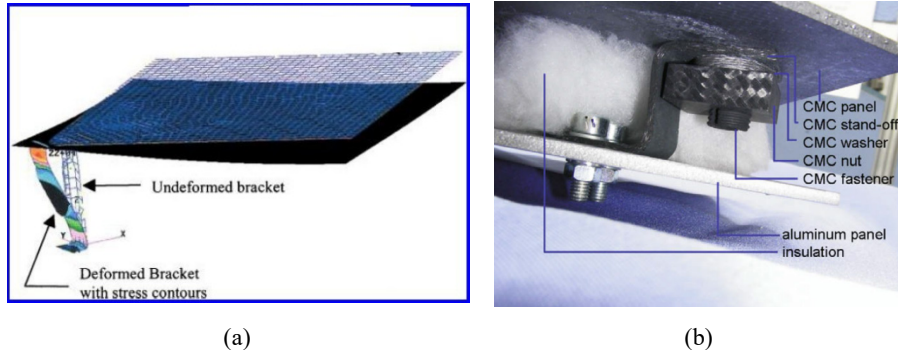
Fig. 1. Z-shaped bracket in thermal protection structure.

In the present work, the heat conduction characteristics and stress distribution patterns of the Z-shaped connecting bracket in thermal protection structures were investi-

gated through simulation. In Section 2, the thermal flux load on aerospace vehicles during reentry into the Earth's atmosphere is addressed briefly. In Section 3, a two-dimensional heat conduction model, considering the thermal radiation interaction between the outer panel and the external environment, is established to analyze the effect of insulation layer thickness on the maximum temperature of the base panel. Then in Section 4, an optimization analysis of the design of the bracket structure is performed. Conclusions are summarized in Section 5.

2 Thermal Flux Load

Most aerospace vehicles experience significant thermal loads during reentry into the Earth's atmosphere, exemplified by a cylindrical mono-stage orbiter with wings in a certain region of the United States [8], as shown in Figure 2. The highest temperatures on the nose and leading edges of the wings reach up to 1, 422 K (2, 100°F). This study focuses on the windward surface of the aircraft subjected to extensive high thermal flux loads, with maximum temperatures reaching 1, 033 K (1, 400°F). The relationship between thermal flux load and time during reentry is depicted in Figure 3 (a), while the relationship between pressure load and time is shown in Figure 3 (b). In Figure 3 (b), pressure refers to the difference between internal and external pressures, with positive values indicating that internal pressure exceeds external pressure. The internal components of spacecraft are commonly made from aluminum alloys. Therefore, the maximum temperature at the bottommost layer of the thermal protection structure should not exceed the highest operational temperature of aluminum alloys, which is typically 450 K [13]. Hence, the external load on the thermal structure comprises actual thermal flux and pressure loads, while the maximum temperature of the cold structure should also not exceed 450 K. As the aerospace vehicle reenters the Earth's atmosphere, the external ambient temperature changes with the spacecraft's speed and surrounding conditions. The variations in external temperature are shown in Table 1.
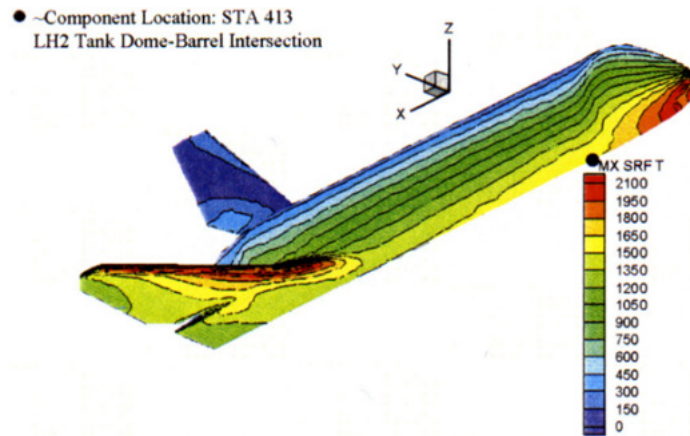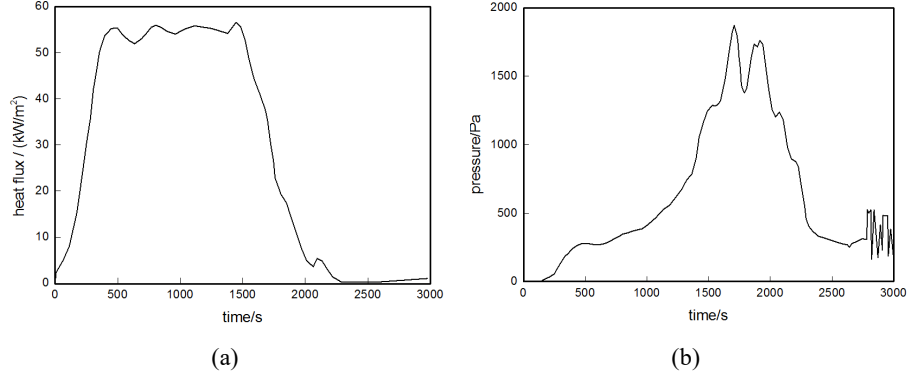

Fig. 2. Distribution of maximum temperatures in aerospace vehicles [8].

Fig. 3. Windward surface thermal flux load and pressure load.

Table 1. External temperature variation during aerospace vehicle reentry into the atmosphere.

Time/s	0	450	1, 575	2, 175	3, 000
Ambient temperature/K	213	243	273	291	295

3   Heat Conduction Analysis

For the thermal protection structure illustrated in Figure 1, consisting sequentially from outer to inner layers of C/SiC composite material panel, Saffil alumina fiber aerogel insulation material, and aluminum alloy bottom panel, the contribution of brackets to local heat conduction processes is minimal. Therefore, the thermal protection system can be simplified to a thermal conduction model of "outer panel − insulation material − bottom panel". Using the windward surface thermal flux load of the aerospace vehicle and the maximum allowable temperature of internal structures as conditions, the minimum thickness of the insulation material can be calculated to determine the thickness parameters of the thermal protection structure.

Saffil alumina fiber can withstand temperatures up to 1, 600°C, with a density of 96 kg/m³, specific heat capacity of 1, 000 $J/kg \cdot K$, and thermal conductivity of 0.08 $W/(m \cdot K)$ [14], disregarding its structural rigidity. Aluminum alloy has an elastic modulus of 70 GPa, thermal conductivity of 100 $W/(m \cdot K)$, and thermal expansion coefficient of 2.3×10^{-5} K^{-1} [15]. The 2D woven C/SiC composite material, with a density of 2.05×10^3 kg/m³ between room temperature and 1, 100 K, exhibits minimal changes in elastic modulus and strength with temperature [16]. Hence, mechanical parameters of C/SiC composite materials in this study are considered temperature-independent, sourced in [17], as listed in Table 2. With an in-plane compressive strength of 409 MPa, tensile strength of 260 MPa, and shear strength of 120 MPa, thermal-related parameters are sourced from [18], as listed in Table 3.

Table 2. Mechanical properties of C/SiC material.

E_1/GPa	E_2/GPa	E_3/GPa	μ_{12}	μ_{13}	μ_{23}	G_{12}/GPa	G_{13}/GPa	G_{23}/GPa
118	118	20.6	0.27	0.07	0.07	21	10.8	10.8

Table 3. Thermal properties of C/SiC composite material.

Temp/K	Specific heat/($J/kg \cdot K$)	Conductivity/($W/(m \cdot K)$)			Mean linear expansion/10^{-6} K^{-1}		
		X	Y	Z	X	Y	Z
293	700	1.25	1.25				
373	710				1.33	1.33	
473	850			1.19	2.42	2.42	1.09
573	970	2.67	2.67	1.00	2.83	2.83	1.19
673	1, 050			0.87	3.16	3.16	1.27
773	1, 100			0.83	3.01	3.01	1.32
873	1, 150	2.13	2.13	0.85	2.99	2.99	1.43
973	1, 220			0.86	3.12	3.12	1.56
1, 073	1, 280			0.87	3.18	3.18	1.68
1, 173	1, 300			0.88	3.29	3.29	1.80
1, 273	1, 290	2.04	2.04	0.89	3.36	3.36	1.93
1, 373					3.47	3.47	
1, 473		2.62	2.62		3.44	3.44	

As temperature increases, the heat flux density due to solid conduction experiences only a slight increase, whereas thermal radiation increases significantly as it is proportional to the fourth power of temperature difference [19]. When temperatures exceed 850°C, thermal radiation becomes the dominant factor. Since the outer panel of the spacecraft remains at high temperatures for most of the reentry phase, convective heat exchange between the outer panel and the external environment, as well as heat conduction, are minimal compared to thermal radiation. Therefore, only thermal radiation is considered in the heat exchange between the outer panel and the external environment.

A 2D model is established, as shown in Figure 4, with the Y-axis direction representing the direction from the inside to the outside of the insulation structure. The outermost layer is C/SiC composite material with a thickness of a=5 mm, followed by an aerogel insulation layer with thickness b, and the innermost layer is an aluminum alloy bottom panel with thickness c=5 mm. Displacement in the Z-direction and rotational degrees of freedom around the X and Y axes are constrained. Since the model only considers heat conduction, no additional displacement constraints are necessary.

The external surface emissivity is 0.8, and the Boltzmann constant is 5.67×10^{-8}. External environmental temperature variations are detailed in Table 1. The thermal flux load is depicted in Figure 3 (a) and is applied to the outermost surface. Despite the low heat flux density of up to 3, 000 seconds, the outermost layer may still exhibit temperatures higher than those of the internal structure due to temperature gradients. Consequently, heat conduction from the outermost layer inward leads to an increase in

the temperature of the aluminum alloy bottom panel. Therefore, the calculation time for this 2D thermal conduction model is set to 5, 000 seconds.

By varying the thickness b of the insulation layer and monitoring the temperature changes on the outer surface of the C/SiC composite material layer and the bottommost temperature of the aluminum alloy panel, the temperature variations of the outer and bottom layers are depicted in Figure 5. From the figures, it is observed that the thickness of the insulation layer has a minimal impact on the maximum temperature of the outermost layer, which reaches 1, 000 K at 550 seconds and maintains around 1, 050 K for the next 600 seconds before gradually decreasing to below 450 K after 3, 000 seconds. The temperature of the bottom panel varies with the thickness of the insulation layer. The decrease in temperature after 3, 000 seconds for different thickness structures of the outermost layer also slows down with increasing insulation layer thickness, attributed to the insulating effect of the insulation layer.

The relationship between the maximum temperature of the bottom panel and the thickness b of the insulation layer is illustrated in Figure 5. The maximum temperature of the bottom panel decreases with the increasing thickness of the insulation layer, and the rate of decrease diminishes as the thickness increases. Therefore, excessively increasing the thickness of the insulation layer to reduce the maximum temperature of the bottom panel may not yield optimal cost-effectiveness. When the insulation layer thickness is increased to 32.5 mm, the maximum temperature of the bottom panel is 447 K, satisfying the temperature requirements for the internal structure.
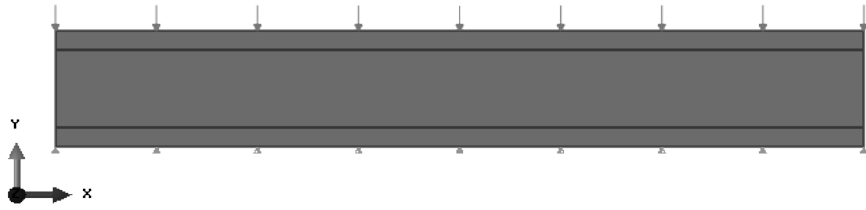
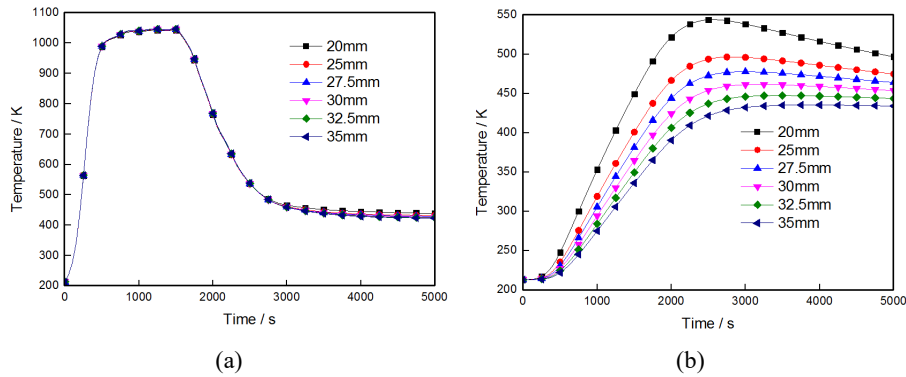

Fig. 4. 2D thermal conduction model.

(a)

(b)

Fig. 5. Temperature variation of outermost layer and bottom panel in 2D model.

Due to the inability of the 2D model to consider the influence of heat conduction perpendicular to the plane, this study uses a structure with an insulation layer thickness of 33 mm as an example. A comparison between the results of 3D and 2D models is conducted to validate the correctness of the 2D model through numerical simulation in 3D. A 3D model is established with an insulation layer thickness of 33 mm, and both the C/SiC outer panel and the aluminum alloy bottom panel have a thickness of 5 mm. The model is without boundary constraints, and the calculation time is set to 5, 000 seconds. The temperatures of the outer surface of the outer panel and the aluminum alloy bottom panel extracted from the 3D model are compared with those from the 2D model, as shown in Figure 6.

| (a) | (b) |
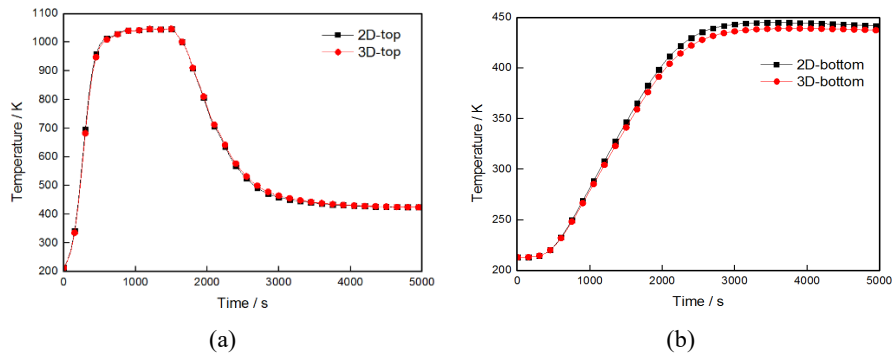
Fig. 6. Temperature comparison between 2D and 3D models.

The comparison shows that the highest temperatures and temperature variation trends of the outermost layer in the 3D model are consistent with those of the 2D model. The temperature trends of the aluminum alloy bottom panel are also consistent, with the highest temperature in the 2D model at 445 K and in the 3D model at 439 K, a difference of 6 K, which is within 2% of the temperature value. The temperature distribution at 3, 000 seconds extracted from both the 2D and 3D models is shown in Figure 7, with a difference of only 1 K at this time. The temperature of the bottom panel is 445 K in the 2D model and 438 K in the 3D model, a difference of 7 K, which also remains within 2% of the temperature value. Therefore, it is concluded that the 2D model can effectively represent the thermal conduction of the 3D structure and the temperature variation of the bottom panel.

Based on the previous analysis, it is evident that after 2, 000 seconds of reentry into the atmosphere, the temperature variations of the outer layer differ with changes in the insulation layer thickness. The choice of insulation material also affects the temperature variations after 2, 000 seconds. Therefore, the temperature variations of the outer surface of the C/SiC layer in the 3D model are compared with the temperature variations on the windward surface of a reentry vehicle as reported in [12]. Figure 7 illustrates this comparison, showing that the calculated results align with the actual trends observed. The maximum temperature values and their durations are consistent, demonstrating the accuracy of the computational approach in this study and its correspondence with the actual temperature variations on the outer surface of the thermal structure.
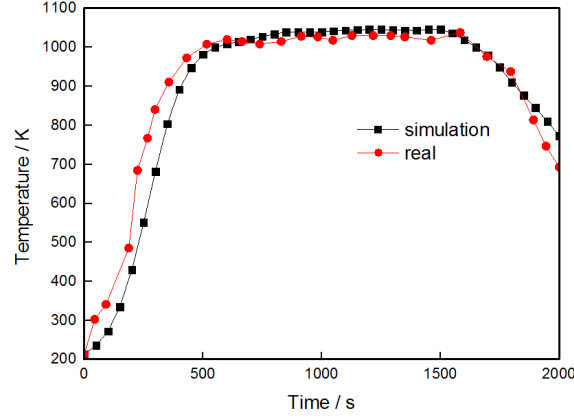
Fig. 7. Comparison of calculated results with actual temperature values.

4 Optimization Analysis of Bracket Structure Form

Due to the discrepancy in temperatures between the outer panel and the internal structure, there exists a thermal expansion mismatch. If the stiffness of the bracket structure perpendicular to the thickness direction is too high, it may resist the deformation of the outer panel excessively, potentially leading to excessive deformation or even plastic deformation. To ensure a certain amount of deformation tolerance for the outer panel in the perpendicular direction, the bracket structure is designed based on the distribution position of brackets described in [5], as shown in Figure 8.
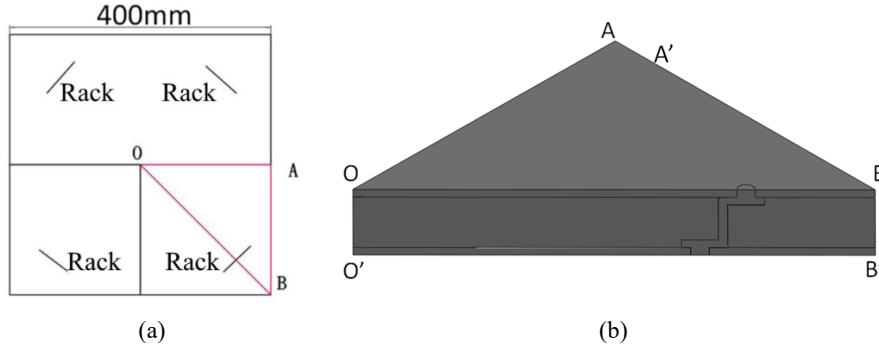

(a)   (b)

Fig. 8. Schematic diagram of bracket positions.

The dimensions of the single thermal protection structure are 400 mm per side, and the brackets are perpendicular to the diagonal. Given the symmetry of boundary conditions, loads, and material properties along the axes of symmetry of the square structure, a 1/8 model is established, as depicted by the red line segment OAB in Figure 8 (b). Here, Points A′ and B′ are located on the underside of the bottom panel, directly below Point A.

The strength of the bolts has been extensively studied in previous sections. In this chapter, the upper and lower ends of the brackets are simplified to cylindrical bodies with a diameter of 10 mm, integrated into the bracket structure. The connection between the bolts and the panels as well as the brackets, is tight; therefore, the edges of the cylindrical bodies are tied to the holes, ensuring that the upper and lower parts of the brackets deform in line with the adjacent panels. The Saffil alumina fiber gel filled between the inner and outer panels is a flexible material, and its stiffness and strength are disregarded in this analysis. Hence, the interaction between the gel and the panels is simplified to a tied connection to facilitate calculation. Within the structure, all other components are treated as contact interactions, with normal direction rigidity and a friction coefficient of 0.2. Thermal impedance between components is not considered. Symmetrical constraints are applied to the OO′B′B and OO′A′A planes, along with constraints on the O′A′B′ plane in the thickness direction displacement and perpendicular displacement of Points O and O′. Thermal flux and pressure loads are applied on the OAB plane.

This study designs four types of brackets based on the Z-shaped structure, as shown in Figure 9, aiming to investigate the influence of different load paths on the maximum stress of the brackets. By comparing the computational results, the optimal structure is selected. The boundary conditions and load settings are consistent with those described earlier, maintaining a vertical distance of 80 mm between the vertical part of the bracket and BB′. Among them, Structure 1, as shown in the right diagram of Figure 8, has a bracket mesh size of 1 mm, a thickness of 5 mm, and a distance of 33 mm between the outer panel and the bottom panel.

(a)

(b)

(c)

(d)
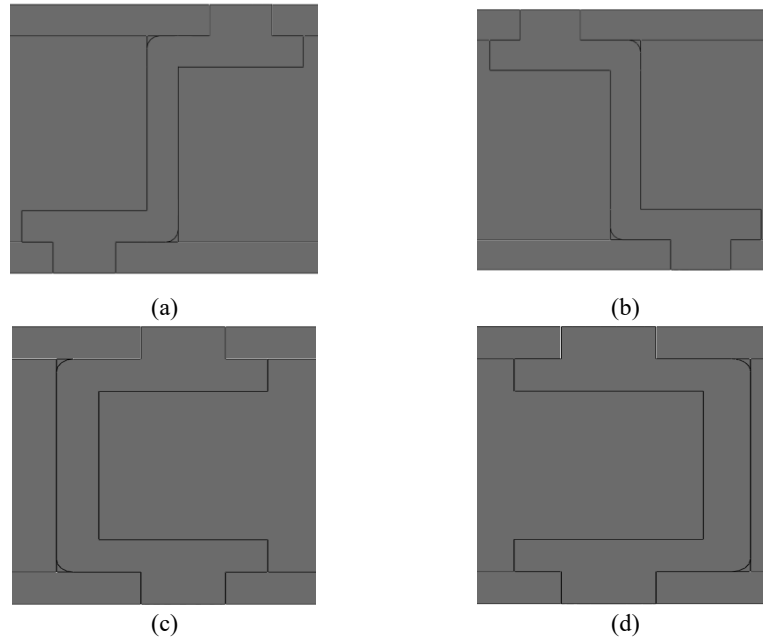
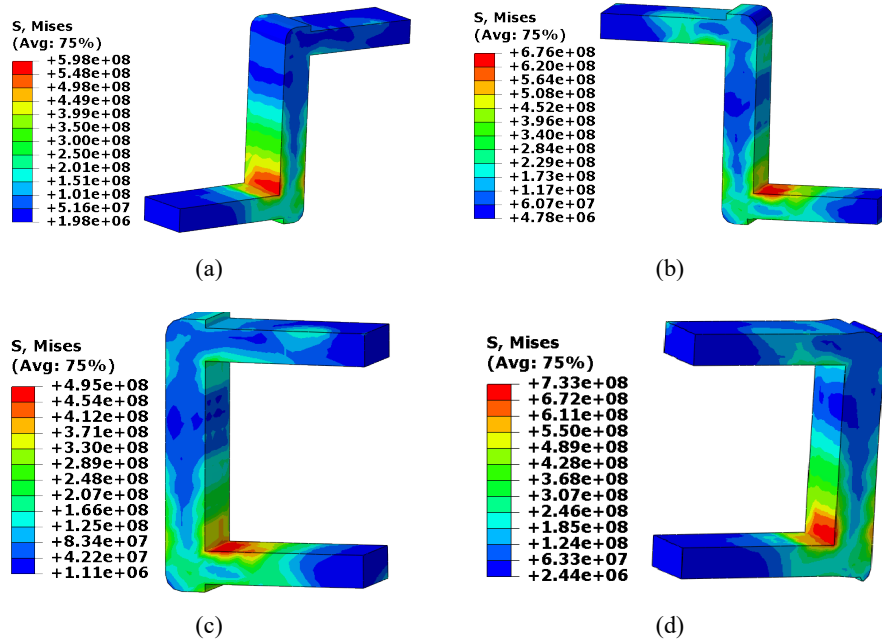**Fig. 9.** Four types of support structures.

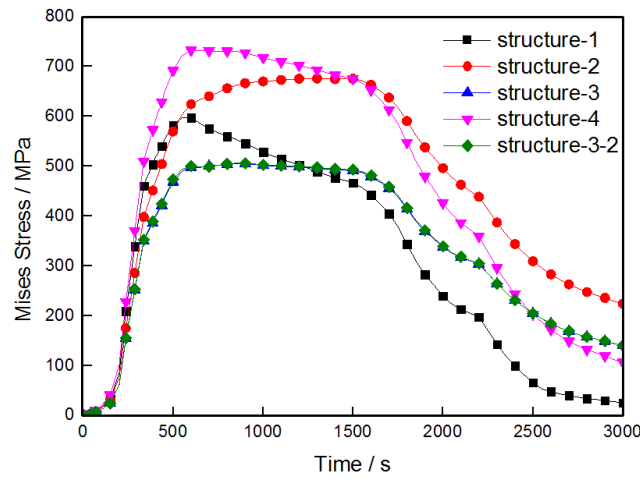Fig. 10. Stress distribution of four types of supports at maximum stress.

Fig. 11. Variation of maximum stress on the support structure.

Four types of support structures' stress distribution at maximum stress are shown in Figure 10. Due to the tie connection between the cylindrical bodies replacing bolts and the threaded holes on the panels, thermal expansion is restricted, causing stress to be misrepresented here. However, this does not affect the structural integrity of the sup-

ports themselves. Hence, the stress contours conceal the cylindrical bodies and the adjacent layer of elements. From the figure, it can be observed that the high-stress regions for all four support structures are located at the corner joints near the base, with Structure Three exhibiting the lowest stress and Structure Four experiencing the highest. The variation of maximum stress over time on the supports is depicted in Figure 11. The curve "Structure-3-2" represents the change in maximum stress on the support structure without additional pressure load for Structure (c). The trends in maximum stress variation on the supports are similar in the initial 500 seconds, followed by a gradual increase to reach peak values, maintaining relatively high levels until around 1, 700 seconds, after which the stress begins to decline.

From the figure, it can be observed that the influence of pressure load on the maximum stress on the supports is relatively small. The primary reason for the presence of high-stress zones on the supports is that the temperature of the outer panel is higher than that of the bottom panel, causing inconsistent deformation in the thickness direction of the structure. As the supports undergo thermal expansion, they resist this inconsistency by bearing complex forces such as bending and compression, resulting in the formation of high-stress zones.

The temperature difference and displacement difference perpendicular to the thickness direction at the bolt holes of the inner and outer panels are shown in Figure 12. A positive temperature value indicates that the temperature at the outer panel bolt hole is higher than that at the bottom panel bolt hole, while a positive displacement value indicates that the displacement at the outer panel bolt hole in the direction perpendicular to the thickness is greater than that at the bottom panel bolt hole. The appearance of displacement difference is mainly due to the temperature gradient in the thickness direction of the structure. The trend of displacement difference in the figure is consistent with the temperature difference, confirming this point. Moreover, the trend of displacement difference aligns with the variation trend of maximum stress on the supports, further demonstrating that the temperature gradient in the thickness direction of the structure is the primary cause of higher stress on the supports.
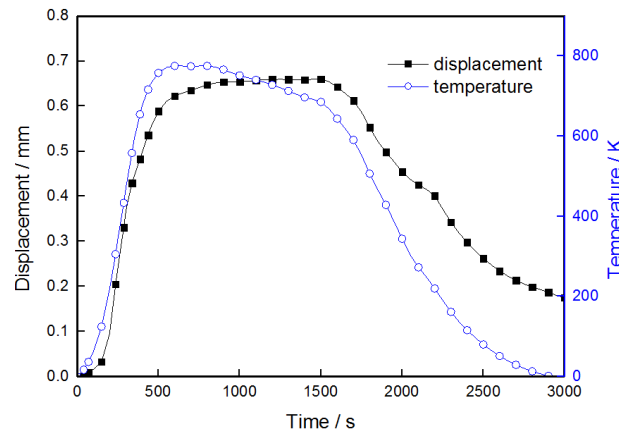
Fig. 12. Displacement difference and temperature difference at bolt holes of inner and outer panels.

5   Conclusion

In this study, a thorough numerical investigation was first conducted on the heat conduction within the thermal protection structure. To this end, a 2D heat conduction model, considering the thermal radiation interaction between the outer panel and the external environment, was established to analyze the effect of insulation layer thickness on the maximum temperature of the base panel. Furthermore, verification of the 2D model was conducted by comparing its numerical results with both the outcomes of a 3D model and actual temperature data. Results revealed that the insulation layer's thickness has a pronounced influence on the temperature of the bottom panel, and specifically, a thickness of 32.5 mm successfully fulfills the temperature requirements for the internal structure.

Secondly, a comprehensive optimization analysis is conducted on the design of the bracket structure utilizing simulations. Four distinct Z-shaped designs were modeled to analyze their stress distribution patterns. Upon examination, high-stress zones were pinpointed at the root corners, exhibiting variations in stress intensities across different designs. Notably, the temperature gradient along the thickness of the structure emerged as the primary contributor to elevated stress levels, offering crucial insights for the design and optimization of thermal protection structures.

The present research provides theoretical support and practical reference for the design and optimization of thermal protection structures in aerospace vehicles. To enhance the support structure's overall performance, future research endeavors might involve a more profound exploration of the impact that additional environmental variables, particularly wind speed and humidity, exert on heat conduction mechanisms and the intricate patterns of stress distribution.

References

1. Wang X., Xu X., and Yang Q. C. (2024). Numerical analysis on the thermal environment of reusable launch vehicle during supersonic retropropulsion. Int. J. Therm. Sci., 198: 108, 857.
2. Ma Z. H. (2004). Performance analysis and research on thermal protection system of reusable launch vehicles (in Chinese). Northwestern Polytechnical University Press, Xi'an.
3. Balesdent M., Brevault L., and Paluch B. (2023). Multidisciplinary design and optimization of winged architectures for reusable launch vehicles. Acta Astronautica, 211: 97-115.
4. Blosser M. L. (2003). Thermal protection systems for reusable launch vehicles. In: 14th Annual Thermal and Fluids Analysis Workshop. Hampton. pp.182-188.

5. Zhang C. Y., Yu P., and Peng H. F. (2024). Prediction of thermal contact resistance for reusable heat-pipe cooled thermal protection system based on an inverse thermos-mechanical coupling method. Renewable Energy, 227: 120, 541.
6. Izaguirre I., Loewenhoff T., and Prado D. J. (2023). Thermal fatigue response of W-Eurofer brazed joints by the application of high heat flux loads. J. Mater. Process. Technol., 319: 118, 056.
7. Zhang S. L., Zhang Z. Y., and Wang Y. (2024). Design and performance verification of thermal protection structure of high-temperature probe in aeroengine. Appl. Therm. Eng., 253: 123, 745.
8. Brociek R., Hetmaniok E., and Napoli C. (2024). Identification of aerothermal heating for thermal protection systems taking into account the thermal resistance between layers. Int. J. Heat Mass Transfer, 218: 124, 772.
9. Zhang X. L., Liang M. K., and Sun F. H. (2024). Thermal insulating performance of thermal protection system with sandwich structure based on Al_2O_3/SiC composites aerogels. Ceram. Int. 50 (18B): 33, 946-33, 952.
10. Sergis A., Hardalupas Y., and Flinders K. (2023). A quantitative study on the thermal performance of self-modified heat transfer surfaces in high heat flux flow systems. Int. J. Therm. Sci., 215: 124, 525.
11. Blosser M. L., Chen R. R., and Schmidt I. H. (2002). Advanced metallic thermal protection system development. In: 40th Aerospace Sciences Meeting & Exhibit. Reno. pp.14-17.
12. Böhrk H. and Beyermann U. (2010). Secure tightening of a CMC fastener for the heat shield of re-entry vehicles. Compos. Struct., 92 (1): 107-112.
13. Blosser M. L. (2000). Advanced metallic thermal protection systems for reusable launch vehicles. University of Virginia Press, Hampton.
14. Tsirogiannis E. C., Psarommatis F., and Prospathopoulos A. (2024). Composite Armor Philosophy (CAP): Holistic design methodology of multi-layered composite protection systems for armored vehicles. Defence Technol., 14: 7-29.
15. Gale W. F. and Totemerier T. C. (2003). Smithells Metals Reference Book, 8th ed. Elsevier, Amsterdarn.
16. Tongji University (2007). Design Specification for Aluminum Alloy Structures (in Chinese).
17. Zhang C., Guan T. H., and Ren T. F. (2022). Influences of SiC infiltration and coating on compressive mechanical behaviors of 2D C/SiC composites up to 1, 600°C at wide-ranging strain rates. J. Eur. Ceram. Soc., 42 (9): 3, 787-3, 801.
18. Zhang B. F. (2010). A Study on the Intrinsic and Service Performance of C/SiC Composite Materials with Precursor Transformation. University of National Defense Technology Press, Changsha.
19. Blosser M. L., Poteet C. C., and Chen R. R. (2004). Development of advanced metallic-thermal-protection system prototype hardware. J. Spacecraft Rockets, 41 (2): 183-194.